DOI: 10.1002/((please add manuscript number))

Article type: Full Paper

Highly Efficient Bifunctional Dielectric Metasurface Enabling Polarization-Tuned Focusing and Deflection for Visible Light

Song Gao, Chul-Soon Park, Sang-Shin Lee, and Duk-Yong Choi*

S. Gao, C.-S. Park, Prof. S.-S. Lee

Department of Electronic Engineering

Kwangwoon University

Seoul, 01897, South Korea

E-mail: slee@kw.ac.kr

Dr. D.-Y. Choi

Laser Physics Centre

Research School of Physics and Engineering

Australian National University

Canberra, ACT 2601, Australia

Dr. D.-Y. Choi

College of Information Science and Technology

Jinan University

Guangzhou, Guangdong, 510632, China

Keywords: bifunctional metasurface; visible metasurface; metalens; light deflection; tunable multifunctional metasurface

Abstract

A multifunctional metasurface has attracted drastically growing interest, serving as a prominent candidate to cope with both device miniaturization and integration. Conventional transmissive bifunctional metasurfaces working for visible light inherently suffer from several demerits owing to the use of geometric phase and spatial multiplexing scheme. Research endeavors have been mainly devoted to the implementation of a static device. In this work, a highly efficient bifunctional dielectric metasurface, taking advantage of a unit cell (UC) the building block of which capitalizes on a nanopost in hydrogenated amorphous silicon, is proposed and experimentally demonstrated to successfully enable polarization-mediated anomalous beam deflection and focusing in the visible band. Through the tailoring of the UC periodicity, we are capable of efficiently tuning the beam deflection angle and focusing distance. For the fabricated sample, the normal transverse-electric incidence within a spectral band from 600 nm to 715 nm is angle-resolved to a single diffraction order via the beam deflection, while a bright line focus is attained at the target focal plane for the normal transverse-magnetic incidence at λ = 650 nm. This work will initiate a positive prospect for the development of high-performance tunable multifunctional metasurfaces.

1. Introduction

Considering the fact that the light wavefront is mediated by the accumulated phase shift over a relatively long propagation distance, conventional optical devices have inevitable shortcomings, including their bulky size, heavyweight, complex shape, and limited performance. Thus, they are neither in compliance with device miniaturization nor suitable to be deployed in integrated photonic systems. A three-dimensional metamaterial, exhibiting exotic material properties that do not exist in nature, offers more flexibility in manipulating electromagnetic waves in an elegant way and providing unprecedented phenomena, such as negative refractive index,[1] perfect lensing,[2] and cloaking.[3] Yet,

the metamaterial is a composite material, which typically involves layered structures, requiring relatively complex fabrication processes; therefore, in practice it is not popular for use in device miniaturization. A metasurface, which is regarded as a two-dimensional metamaterial, has recently emerged as a prominent alternative to the metamaterial because of its ability to cope with the aforementioned issues. An optical metasurface is particularly supposed to engage subwavelength-spaced metallic or dielectric nanostructures (meta-atoms), whose size, shape, and orientation can be adjusted to facilitate the manipulation of the light amplitude, phase, and polarization. In light of these salient features, a plethora of ultra-thin optical devices, including beam deflectors,[4,5] metalenses,[6,7] waveplates,[8,9] and meta-holograms,[10,11] were extensively studied.

So far, the majority of the invented metasurfaces have exhibited a single, predetermined function. Because of the ever-growing demand for improving the capacity for data storage and information management, it is highly desirable to have a single device with versatile functions. This was recently made possible by the development of a metasurface in which multiple functions can be realized by controlling the polarization, wavelength, and incidence angle.[12-20] For instance, by varying the helicity of incident circularly polarized (CP) light, two dissimilar holograms can be reconstructed based on a single metasurface that contains two sets of merged hologram data.[19] As different phase profiles carrying different information can be encoded in the two orthogonal polarizations, such bifunctional metasurface may find applications in data storage, information encryption, and anti-counterfeiting. A monolayer of gap-plasmonic metasurface can deflect and focus normally incident light toward different directions and in different focal planes, respectively, depending on the linear polarization of incident light.[12,14] Previous metasurfaces have offered identical or similar functions, but another category of multifunctional metasurface, which can perform dissimilar functions, is desperately awaited for the advantages it will offer in terms of the device integration.[21] Such metasurfaces could be utilized to substantially reduce the elements' footprint and thus integrate multiple imaging systems or optical communication systems. This has been asserted in the microwave,[22,23] and visible band.[24-26] Based on the dielectric/metal-dielectric-metal configurations, however, they are mostly limited to operating in reflection mode.[24-26] Transmissive bifunctional metasurfaces were reported in the microwave,[22,23] terahertz,[27] mid-infrared,[28] near-infrared,[15] and visible regimes.[29,30] In particular, the visible bifunctional plasmonic metasurfaces count on the Pancharatnam-Berry (P-B) phase so as to manipulate the wavefront of CP light. Despite its intrinsic wavelength-independent or dispersion-free characteristics, leading to the broadband operation, the P-B phase is deemed to be susceptible to several limitations. For a metasurface capitalizing on the P-B phase, the incident CP light is known to be scattered into waves of both the same and opposite polarizations.[31] The abrupt phase shift useful for wavefront shaping can be readily accomplished by simply rotating the orientation of the meta-atoms. However, it is solely effective for the CP light with the opposite polarization. The useful transmitted CP light corresponding to the opposite polarization results in a limited polarization conversion efficiency of 25%.[32] Because the metasurface is formed via a spatial multiplexing of double metasurfaces delivering distinct functionalities, a functional crosstalk may potentially arise because one function tends to add background noise to another.[21]

In addition to the progress in the development of a multifunctional metasurface whose functional roles are "static", a colossal amount of efforts has been devoted to the creation of tunable or reconfigurable metasurfaces for manipulating the electromagnetic wave in a tunable manner. This has been achieved by applying external stimuli, such as the electric bias voltage,[33-35] heat,[36-39] and elastic force,[40] to the metasurfaces that incorporate a transparent conducting oxide, phase-change material,

and elastic material, respectively. The former two approaches were substantiated in the spectral band covering the millimeter waves, mid-, and near-infrared. The third scheme is currently thought to be the most feasible way of producing a tunable metasurface for wavefront shaping in the visible band. Nonetheless, the relevant stretchable metasurface relies on the use of the P-B phase, suffering from its disadvantages including the limited operation for cross-polarized CP light with low efficiency, as mentioned above.[41,42] To date, all the proposed tunable metasurfaces are just able to render a single functionality.

In this paper, we propose and develop a highly-efficient bifunctional dielectric metasurface that renders polarization-tuned beam deflection and focusing in the visible regime. The meta-atom constituting the metasurface unit cell (UC) is made of a hydrogenated amorphous silicon (a-Si:H) nanopost in a rectangular shape, imparting polarization-selective phase shifts for implementing the two functions. For that purpose, we first explored the relation between the geometric dimension of the nanopost and the polarization-dependent phase shifts. For the constructed bifunctional metasurface, a theoretical analysis shows that, upon normal incident light with the designated polarizations, not only anomalous beam deflection but also light focusing, exhibiting a high efficiency and negligible functional crosstalk, can be visualized through the simulated field profiles. As against conventional polarization beam splitting meta-devices, whose efficiency can be predicted by a few meta-atoms, the beam deflection efficiency of the proposed bifunctional metasurface is critically dictated by the efficiency of every single meta-atom. The phase delays associated with each nanopost is further examined and found to exhibit insignificant reliance on the periodicity of the UC. The inspection of the tightly confined optical fields inside the nanoposts helps support the comprehension of the underlying mechanism. The UC periodicity can be used to concurretnly and efficiently adjust the angle of light deflection and focusing distance. For a manufactured bifunctional metasurface, the performance has been meticulously inspected in terms of the beam deflection and focusing, by monitoring the angular distribution of the far-field intensity and the light intensity images at different positions from the sample. The reliability of the proposed approach is proven by the excellent consistency between the simulation and measurement results.

2. Results and Discussion

To achieve disparate wavefront modulations, a bifunctional metasurface is required to efficiently impart two distinct spatial phase distributions without incurring profound functional crosstalk, which means that one function that is on duty is rarely adversely affected by the other function that is off duty. The conventional advanced transmissive bifunctional metasurface, operating in the visible spectral band, chiefly relied on a spatial multiplexing scheme and, thus it was inevitably susceptible to functional crosstalk and limited efficiency.[29] Our bifunctional metasurface has been conceived based on the fact that an individual dielectric meta-atom induces flexible phase delays upon incident

light depending on the polarization.[15] It is noted the crosstalk issue may be mitigated by an off-axis illumination methodology.[43] A schematic of the proposed bifunctional metasurface is illustrated in **Figure 1a**. For incident light with the electric field aligned parallel to the x-axis (TE polarization) or y-axis (TM polarization), the metasurface acts as an anomalous beam deflector and cylindrical lens, respectively. The UC of the proposed metasurface consists of a rectangular a-Si:H nanopost atop a silicon dioxide (SiO_2) substrate, as shown in the magnified schematic in Figure 1a. With regard to the UC, the optical phase shift imposed by the Si nanopost is expected to fulfill a 2π span, usually through the tailoring of its cross-sectional dimension. Toward that end, with the assistance of the finite difference time domain (FDTD) method (FDTD Solutions, Lumerical, Canada), the transmission amplitude and phase distributions are examined as a function of the widths of the nanopost, including d_x and d_y. The proposed metasurface is designed to work at a visible wavelength of λ_0 = ~690 nm. The period of the UC is given by P = 240 nm (~0.35λ_0), while the a-Si:H nanopost features a subwavelength thickness of t = 320 nm. As displayed in Figure 1b and 1c, it is implied from the calculated transmission amplitude (A_{TE}) and phase (φ_{TE}) that by selecting a collection of nanoposts with proper dimensions, a full phase tuning of 2π can be obtained for the TE incident polarization in a highly efficient manner. Similarly, the results are explored for the TM incident polarization, as detailed in Figure S1 in Supporting Information. In light of the rectangular shape of the nanopost, the profiles of the transmission amplitude and phase corresponding to the TE and TM polarizations are in mirror symmetry with respect to the diagonal line for $d_x = d_y$.[15] To establish the required phase profiles relating to the TE and TM cases, a conventional eight-level phase modulation, which is appropriate for enabling wavefront manipulation, has been chosen. Eventually, sixty-four nanoposts

with varying widths are employed to arbitrarily derive a polarization-sensitive wavefront (Figure S1 in Supporting Information).

A bifunctional metasurface involving an array of 208 by 208 meta-atoms has been suggested to accomplish polarization-controlled beam deflection and focusing, thus demonstrating that a bifunctional metasurface capitalizing on the proposed nanoposts is empowered to lead to two distinct wavefront modulations,. **Figure 2a** displays a portion of the nanopost-based metasurface. A group of 208 nanoposts in each column, arranged along the x-axis, may be regarded as a supercell, delivering a hyperbolic phase profile for TM incidence. The supercell is periodically duplicated along the y-axis to invoke a line focusing for the TM case. With regard to the beam deflection, which is achievable for the TE polarization, the supercell may be treated as comprising 26 sub-supercells, with each sub-supercell engaging eight nanoposts that are required to give a linearly varying 2π phase shift. For the TM polarization, with respect to the central position $x_0 = 0$ in the middle of the supercell, the 208 meta-atoms belonging to a specific line stretching along the x-axis are deemed to collectively impart a hyperbolic phase profile $\varphi(x)|_{TM} = \frac{2\pi}{\lambda_0}\left(f_0 - \sqrt{(x-x_0)^2 + f_0^2}\right)$. Hence the light beam is focused at a focal length f_0, which is designed to be 20 μm, translating into a relatively large numerical aperture (NA) of 0.78. Both theoretical and simulated phase profiles are illustrated in Figure 2b and 2c. Under normally incident TE polarized light, the wavefront is simulated, and this is depicted in Figure 2d, where an obliquely tilted wavefront is observed immediately after the metasurface. In the case of the TM incidence, the light focusing effect is readily inferred from the simulated electric field intensity profile in the x-z plane, as shown in Figure 2e.

From the perspective of the simulated field profiles, the proposed bifunctional metasurface is anticipated to be invulnerable to serious functional crosstalk. For the performance in terms of individual functions, the angle of beam deflection is derived from the well-known generalized Snell's law, which is tantamount to the diffraction equation.[12] The deflection angle is estimated to be 21.10° in simulation (**Figure 3a**), which closely mimics the theoretically calculated angle of 21.06°. The previously reported bifunctional metasurface, rendering two similar actions of polarization-controlled beam deflection, usually comprises a multitude of identical sub-supercells that are periodically arranged along the lateral direction.[12] The corresponding beam deflection efficiency can be predicted from the individual sub-supercell possessing a couple of meta-atoms. Meanwhile, for the proposed bifunctional metasurface, the overall beam deflection is keenly dictated by the deflection capability of the 26 sub-supercells. It is noted that the efficiency of each sub-supercell hinges on the cross-sectional dimensions of its nanopost elements. Figure 3b depicts the simulated total transmission (T_t), in conjunction with the absolute (T_1) and relative ($\eta = T_1 / T_t$) deflection efficiency for a given sub-supercell. Fluctuating amplitude and imperfect phase shift, in conjunction with nonuniform phase deviations across the nanoposts, combine to cause variations in the efficiency. For the 26 sub-supercells, the averaged total transmission is 85%, while the absolute and relative deflection efficiencies are approximately 72% and 85%, respectively. The non-unity total transmission may be attributed to the absorption in the a-Si:H layer as well as the reflection from the air-Si and Si-SiO_2 interfaces. As shown in Figure 2d, the substantially planar wavefront for the transmitted light, free of any serious distortion, complies with the fact that the light energy (Figure S2 in Supporting Information) is mostly preserved in the anomalous deflection mode (Figure 3a). The total transmission and absolute deflection efficiency of the bifunctional metasurface under the TE

incidence are around 83% and 72%, respectively, while ~12% of the incident light is reflected. The corresponding calculated absorption is ~5%, according to the law of energy conservation. In addition, Figure 3c shows that the anomalous deflection in connection with each sub-supercell can be considerably effective in the spectral band from λ = 630 nm to 750 nm. As a beam deflector, its broadband operation is consistent with the previous polarization insensitive metasurface.[44] For the normal TM incidence, the metasurface serves as a cylindrical metalens, and the light transmitted through it is focused 20 μm away from the metasurface, as intended (Figure 2e). The cylindrical metalens forms a spot with an estimated full-width at half-maximum (FWHM) of 485 nm (~0.7λ), emulating the diffraction-limited spot size of 442 nm (0.5λ / NA). Further simulation reveals that the total transmission, reflection, and calculated absorption in this case are 69%, 19%, and 12%, respectively. The unequal absorption or reflection level compared to the case in TE polarization is likely due to the dissimilar dimension of the nanoposts. The focusing efficiency, which is defined as the fraction of the incident light that passes through a rectangular aperture at the focal plane (z = 20 μm) with a width equal to six times the FWHM, is calculated to be ~60%.[14] As shown in Figure 3d, the intensity is distributed along the z-axis at the center (x = 0) of the metasurface with the wavelength, guaranteeing that the beam focusing is effective over a relatively broad spectral band. Unlike the achromatic metalens, whose chromatic dispersion has been deliberately corrected, the focal length of the proposed metasurface changes depending on the wavelength regime of concern.[45,46]

For the proposed dielectric metasurface, it is believed that the Si nanopost constituting the UC plays a role as a truncated waveguide and permits a low-quality-factor Fabry-Pérot resonance, which is relevant to the Fresnel reflections at either end of the waveguide.[15] Given a sufficiently thick Si

nanopost, the high index contrast between a-Si:H ($n \approx 4.077 + 0.005i$) and the surrounding air ($n = 1$) is presumed to render an entire 2π phase shift when the waveguide effective index is tailored by simply altering its widths.[47,48] The rectangular-shaped nanopost is supposed to exhibit two distinct effective indices hinging on the incident polarization. This causes the phase shift imposed by the nanopost to become polarization dependent. It is reported that a larger nanopost can lead to a higher effective index, thus introducing a larger phase shift.[49] This interpretation is highly consistent with the simulation results shown in Figure 1c. As an example, Figure 3e depicts the magnetic field ($|H_y|$) of the two sub-supercells (#10 and #11) in the designed metasurface for normally incident TE polarized light. Resonance phenomena pertaining to the waveguide-like cavities indicate that the optical fields are primarily confined to the nanoposts. As a consequence, the local phase shift is dominantly governed by the nanopost itself, being hardly affected by its neighboring nanoposts and the periodicity of the UC.[44,50,51]

To analyze the impact of the UC periodicity on the local phase shift, further simulatios were performed. **Figure 4a** depictes a case in which a symmetric nanopost with equal widths is incorporated into a single UC. As shown in Figure 4b, for a constant nanopost width, the transmission phase is almost invariant to the periods of interest. The corresponding amplitude profile causes no profound variations, as portrayed in Figure S3 in the Supporting Information. These conspicuous features, especially the period-insensitive phase shift, have been capitalized on for building a focus-tunable and polarization-insensitive metalens, operating in the near-infrared regime.[40] For the proposed bifunctional metasurface, a similar effect (i.e., period-insensitive phase shift) has been witnessed. For instance, Figure S4 in Supporting Information depicts the simulated electric field profiles for eight meta-atoms in the sub-supercell (#10) when the periodicity of the UC

is set to 240 nm (original design) and 280 nm. It is found that for both TE and TM incidence, the UC periodicity has no significant influence on the phase delay. This appealing feature opens a new avenue for creating a reconfigurable bifunctional metasurface, which allows for the tuning of the beam deflection angle and focal length. If the low-index substrate for the designed metasurface is replaced with a flexible elastic material, such as polydimethylsiloxane (PDMS),[40-42] or electroactive polymer (artificial muscle),[52] the simultaneous realization of tunable beam deflection and zoom lensing might be feasible with a single metasurface. As a proof of concept, we theoretically scrutinized the performance of the bifunctional metasurface at the designed wavelength when the UC periodicity is altered from 240 nm to 300 nm in steps of 10 nm. Under normal TE incidence, the anomalous beam deflection gradually decreases in angle from 21.1° to 16.7° as the UC periodicity increases (Figure 4c). In the meantime, the total transmission is stably maintained over 80% (Figure 4d) when the transmitted light energy is largely preserved in the desired anomalous deflection mode (inset). The simulated focal length for the incident TM polarization is plotted in Figure 4e. The focal length rises from 20 μm to 33.8 μm as the UC peridicity increases. The corresponding NAs, marked in the figure, remain relatively large. Further details on the simulated beam focusing effect and derived beam spot can be found in Figure S5 in Supporting Information, which shows that a diffraction-limited focal spot is retained across all the cases. As plotted in Figure 4f, the total transmission increases slightly with the UC periodicity, with the focusing efficiency staying in the vicinity of 60%. For the designed bifunctional metasurface made of high-index a-Si:H, the beam deflection and focusing can be made possible even when the a-Si:H nanoposts are immersed in a flexible substrate of PDMS ($n = 1.4$) instead of a rigid substrate in SiO_2 ($n \sim 1.5$). Relevant simulation results are included in Figure S6 in Supporting Information. Note that the proposed metasurface is different

from the previously reported reflective phase-shaping device that taps into a high-contrast grating (HCG).[53,54] The reflective HCG device, whose phase tuning is subject to the inter-grating coupling, usually imprints a desired phase profile by adjusting the grating width and the periodicity of the UC. Besides the change in the grating size, the local phase shift is influenced by the gap between the gratings. Additionally, a Huygens' metasurface, drawing upon identical low-aspect-ratio dielectric meta-atoms, can also exhibit a full-2π phase coverage via the periodicity of the UC lattice.[55,56] A spatial multiplexing of both the period-dependent and period-independent meta-atoms in an elastic material is expected to bring extra freedom in metasurface design.

In a bid to experimentally validate the abovementioned claims, a bifunctional metasurface has been manufactured via electron beam lithography (EBL) and lift-off processes (more details are elaborated in the Experimental Section).[57] Dimensions of the a-Si:H nanoposts are kept the same as in the case of the bifunctional metasurface discussed in Figure 2 (designed with P = 240 nm), while the UC periodicity of the fabricated sample is chosen to be 280 nm. **Figure 5a** shows an optical image and scanning electron microscope (SEM) image of the fabricated metasurface. For normal TE incidence, a Fourier-transform-based angle-resolved spectroscopy (FT-ARS) measurement was first carried out to obtain the far-field intensity distributions from the light source (I_{in}) and sample (I_{out}). In accordance with the generalized Snell's law or the diffraction equation, the desired anomalous deflection mode is equivalent to the first diffraction order (m = 1). The normalized far-field intensity (I_{out} / I_{in}) displayed in Figure 5b implies that the transmitted light from the fabricated metasurface is chiefly preserved in the first diffraction order, which is effective over a relatively broad band, from λ = 600 nm to 715 nm. However, light energy is scarcely conserved in the m = -1 order. The observed intensity distribution at the wavelength of 690 nm exhibits a maximum at the angle of 18.00°, nearly

matching the simulated deflection angle of 17.94°. The relationship between the wavelength and diffraction angle is then calculated and marked by the dashed line in Figure 5b, featuring good correlations between the calculation and measurement. In an effort to assess the beam focusing for normal TM incidence, the custom-built setup shown in Figure 5c is prepared. A supercontinuum laser (NKT "SuperK compact") equipped with a collimator emits broadband light, which passes through a linear polarizer (GTH10N-A, Thorlabs) and narrowband filter. Subsequently, it normally impinges on the prepared sample. Noting that the metasurface can operate in a wide band, a filter with a center wavelength at 650 nm (a line-width of 10 nm) is used to characterize the beam focusing. A customized imaging system that includes a microscope objective lens, tube lens, and charge coupled device, is adopted to record the intensity pattern after the light is transmitted through the sample. A series of images (intensity distributions in the x-y plane) are taken by translating the imaging system along the optic axis (z-axis) in increments of 1 μm. Figure 5d presents two examples of intensity distributions in the sample plane (z = 0) and the metalens focal plane (z = 32 μm). Figure 5e displays the intensity profile in the x-z plane relating to the light trajectory when the intensity in the transversal line (along the x-axis) is taken across the center of all the recorded images. The light beam gradually converges and becomes focused at z = 32 μm, which is in decent agreement with the simulated focal length of ~31 μm for λ = 650 nm. The longitudinal focus profile extends approximately from z = 30 μm to 37 μm and the horizontal beam width as observed at z = 32 μm is estimated to be around 830 nm, which is larger than the simulated result yet still corresponds to the wavelength scale. The focus profile stretches slightly longer than in the simulation, which might be ascribed to the non-zero spectral bandwidth of the filter and the dispersion of the metasurface.[58] To practically explore the focusing efficiency, the imaging system

shown in Figure 5c should be supplanted with a power monitor. Moreover a rectangular-shaped pinhole with a proper width needs to be particularly placed at the focal plane of the metalens.[59] The experimental restrictions prohibited us from checking the focusing efficiency of the bifunctional metasurface. The discrepancy between the measurement and simulation results may be due to probable imperfections during the fabrication of the a-Si:H structure, such as the surface/edge roughness and dimension deviation. Nevertheless, the transmitted light that mainly resides in the first diffraction order for the TE incidence, alongside the observed light intensity image with a bright line focus at the focal plane for the TM incidence, helps validate the prominent features of the fabricated sample. We investigated into the robustness of the proposed metasurface with respect to the structural tolerance. It was numerically observed that when the dimensions of the nanoposts are particularly varied from -20 nm to +20 nm, the performance of the metasurface in terms of the beam deflection and focusing is stably maintained, yet the efficiency is relatively noticeably affected. The corresponding simulation results are shown in Figures S7 and S8 in Supporting Information. Leveraging meta-atoms based of lossless dielectrics such as titanium dioxide, gallium nitride, and silicon nitride, we can concretely envision the embodiment of advanced bifunctional metasurfaces operating at shorter visible wavelengths.[6, 60, 61]

3. Conclusion

A highly-efficient transmissive bifunctional metasurface, empowering polarization-tuned focusing and deflection for visible light, was successfully presented. The polarization-mediated phase manipulation was completely fulfilled through the incorporation of a rectangular a-Si:H nanopost in

each UC of the metasurface. The nanoposts constituting the bifunctional metasurface were devised in a sophisticated manner to impart a linear and hyperbolic phase profile for the TE and TM polarization, respectively. The high performance of the proposed bifunctional metasurface in the visible regime can be assured, as is highlighted by the simulation results, including the obliquely transmitted light with a well-defined planar wavefront for normal TE incidence and a subwavelength diffraction-limited focal spot at the desired focal plane for TM incidence, along with a total transmission level ranging up to 83%. The optical fields, which are revealed to be exclusively confined in the nanopost, give rise to a decently stable phase shift through the tailoring of the UC periodicity. This fascinating feature facilitates the tuning of the beam deflection angle and focal length, as demonstrated in simulations. A metasurface was created in a practical manner with the help of standard EBL, metal lift-off, and plasma etching processes. The high performance of the sample was confirmed by checking the angular distribution of the far-field intensity and the light intensity images carried out with the FT-ARS technique and custom-built setup. By imbedding the proposed nanoposts in elastic materials, we will be able to concoct a versatile meta-device, featuring affordable miniaturization and enhanced efficiency.

Experimental Section

Fabrication: The preparation of the bifunctional metasurfaces started with acetone/IPA/deionized water cleaning of a slide glass to promote the adhesion between the glass substrate and an a-Si:H layer. A 320-nm thick a-Si:H film was then deposited on the substrate via plasma-enhanced chemical vapor deposition (Plasmalab 100 from Oxford) using optimized conditions derived in the previous

work.[57] After spin coating of an electron beam resist (ZEP520A from Zeon Chemicals), a thin layer of e-spacer 300Z (Showa Denko) was introduced to prevent charging during subsequent electron beam exposure. The metasurface pattern was then formed using an electron beam writer (EBL, Raith150) and subsequent development in ZED-N50. Next, a 60-nm thick Al layer was deposited by e-beam evaporation (Temescal BJD-2000), accompanied by a lift-off process by soaking the sample in a resist remover (ZDMAC from ZEON Co.). An array of remaining rectangular Al patterns was used as the etch mask to transfer the designed pattern into the a-Si:H film through fluorine-based inductively coupled plasma-reactive ion etching (Oxford Plasmalab System 100). The etching conditions were optimized to ensure a highly anisotropic profile for the a-Si:H layer. Finally, wet etching was used to remove the residual Al etch mask. Note that the properties of the amorphous Si are deemed to depend on the hydrogen concentration induced under different deposition conditions. For our used a-Si:H, the bandgap is 1.73eV (corresponding to 717 nm).[57] The extinction coefficient is around 0.036 at the wavelength of 650 nm, which translates into 18% absorption in the case of a 320-nm thick film. However, the areal fraction of the a-Si:H should be taken into account when the metasurface pattern is produced in the film.

Numerical Simulation: The 2D amplitude and phase contour maps shown in Figure 1b and 1c are calculated in FDTD Solutions by scanning the cross-sectional dimensions of a single a-Si:H nanopost, which is sitting atop the SiO_2 substrate in a UC. For the simulations, periodic boundary conditions are applied along both the x- and y-axes, while perfect matched layer (PML) boundary conditions are imposed along the z-axis. The UC is illuminated by a plane wave source at λ = 690 nm, which is positioned inside the substrate, while a power monitor (in the x-y plane) is positioned in the air to trace the amplitude and phase of the transmitted light. For the simulations associated with the

anomalous beam refraction and focusing, one supercell containing 208 nanoposts with designed lateral dimensions has been constructed through a script. Boundary conditions along the y- and x-axis are set to be periodic and PML. The computation region along the x-axis is 1 μm larger than the metasurface. A total-field scattered field (TFSF) source is utilized to feed the metasurface area from the SiO_2 side.

Supporting Information

Supporting Information is available from the Wiley Online Library or from the author.

Acknowledgements

This work was supported by National Research Foundation of Korea (NRF) grants funded by the Korea government (MSIP) (No. 2016R1A2B2010170) and the Ministry of Education (No. 2018R1A6A1A03025242). The work was partly supported by the Australian Research Council Future Fellowship (FT110100853, Dr. Duk-Yong Choi) and was performed in part at the ACT node of the Australian National Fabrication Facility. The authors thank Prof. L. Shi, Prof. J. Zi, and Y. Zhang from Fudan University and Dr. H. Yin from Ideaoptics Inc., for their help with the Fourier-transform-based angle-resolved spectroscopy (FT-ARS) measurements.

Received: ((will be filled in by the editorial staff))
Revised: ((will be filled in by the editorial staff))
Published online: ((will be filled in by the editorial staff))

References

[1] V. G. Veselago, *Sov. Phys. Usp.* **1968**, *10*, 509.

[2] J. B. Pendry, *Phys. Rev. Lett.* **2000**, *85*, 3966.

[3] R. Liu, C. Ji, J. J. Mock, J. Y. Chin, T. J. Cui, D. R. Smith, *Science* **2009**, *323*, 366.

[4] N. Yu, P. Genevet, M. A. Kats, F. Aieta, J. P. Tetienne, F. Capasso, Z. Gaburro, *Science* **2011**, *334*, 333.

[5] X. Ni, N. K. Emani, A. V. Kildishev, A. Boltasseva, V. M. Shalaev, *Science* **2012**, *335*, 427.

[6] M. Khorasaninejad, W. T. Chen, R. C. Devlin, J. Oh, A. Y. Zhu, F. Capasso, *Science* **2016**, *352*, 1190.

[7] S. Wang, P. C. Wu, V.-C. Su, Y.-C. Lai, M.-K. Chen, H. Y. Kuo, B. H. Chen, Y. H. Chen, T.-T. Huang, J.-H. Wang, R.-M. Lin, C.-H. Kuan, T. Li, Z. Wang, S. Zhu, D. P. Tsai, *Nat. Nanotechnol.* **2018**, *13*, 227.

[8] F. Ding, Z. Wang, S. He, V. M. Shalaev, A. V. Kildishev, *ACS Nano* **2015**, *9*, 4111.

[9] Z. H. Jiang, L. Lin, D. Ma, S. Yun, D. H. Werner, Z. Liu, T. S. Mayer, *Sci. Rep.* **2014**, *4*, 7511.

[10] B. Wang, F. Dong, Q.-T. Li, D. Yang, C. Sun, J. Chen, Z. Song, L, Xu, W. Chu, Y.-F. Xiao, Q. Gong, Y. Li, *Nano Lett.* **2016**, *16*, 5235.

[11] W. T. Chen, K.-Y. Yang, C.-M. Wang, Y.-W. Huang, G. Sun, I.-D. Chiang, C. Y. Liao, W.-L. Hsu, H. T. Lin, S. Sun, L. Zhou, A. Q. Liu, D. P. Tsai, *Nano Lett.* **2014**, *14*, 225.

[12] A. Pors, O. Albrektsen, I. P. Radko, S. I. Bozhevolnyi, *Sci. Rep.* **2013**, *3*, 2155.

[13] M. Farmahini-Farahani, H. Mosallaei, *Opt. Lett.* **2013**, *38*, 462.

[14] S. Boroviks, R. A. Deshpande, N. A. Mortensen, S. I. Bozhevolnyi, *ACS Photonics* **2018**, *5*, 1648.

[15] A. Arbabi, Y. Horie, M. Bagheri, A. Faraon, *Nat. Nanotechnol.* **2015**, *10*, 937.

[16] S. M. Kamali, E. Arbabi, A. Arbabi, Y. Horie, M. Faraji-Dana, A. Faraon, *Phys. Rev. X* **2017**, *7*, 041056.

[17] E. Arbabi, A. Arbabi, S. M. Kamali, Y. Horie, A. Faraon, *Optica* **2016**, *3*, 628.

[18] E. Arbabi, A. Arbabi, S. M. Kamali, Y. Horie, A. Faraon, *Sci. Rep.* **2016**, *6*, 32803.

[19] D. Wen, F. Yue, G. Li, G. Zheng, K. Chan, S. Chen, M. Chen, K. F. Li, P. W. Wong, K. W. Cheah, E. Y. B. Pun, S. Zhang, X. Chen, *Nat. Commun*. **2015**, *6*, 8241.

[20] Q. Wang, X. Zhang, E. Plum, Q. Xu, M. Wei, Y. Xu, H. Zhang, Y. Liao, J. Gu, J. Han, W. Zhang, *Adv. Opt. Mater.* **2017**, *5*, 1700277.

[21] S. Tang, T. Cai, H.-X. Xu, Q. He, S. Sun, L. Zhou, *Appl. Sci.* **2018**, *8*, 555.

[22] T. Cai, S. Tang, G. Wang, H. Xu, S. Sun, Q. He, L. Zhou, *Adv. Opt. Mater.* **2017**, *5*, 1600506.

[23] T. Cai, G. Wang, H. Xu, S. Tang, H. Li, J. Liang, Y. Zhuang, *Ann. Phys. (Berlin)* **2017**, *530*, 1700321.

[24] Z. Shi, M. Khorasaninejad, Y.-W. Huang, C. Roques-Carmes, A. Y. Zhu, W. T. Chen, V. Sanjeev, Z.-W. Ding, M. Tamagnone, K. Chaudhary, R. C. Devlin, C.-W. Qiu, F. Capasso, *Nano Lett.* **2018**, *18*, 2420.

[25] C. Zhang, F. Yue, D. Wen, M. Chen, Z. Zhang, W. Wang, X. Chen, *ACS Photonics* **2017**, *4*, 1906.

[26] F. Ding, R. Deshpande, S. I. Bozhevolnyi, *Light Sci. Appl.* **2018**, *7*, e17178.

[27] H. Zhang, X. Zhang, Q. Xu, C. Tian, Q. Wang, Y. Xu, Y. Li, J. Gu, Z. Tian, C. Ouyang, X. Zhang, C. Hu, J. Han, W. Zhang, *Adv. Opt. Mater.* **2018**, *6*, 1700773.

[28] F. Zhang, H. Yu, J. Fang, M. Zhang, S. Chen, J. Wang, A. He, J. Chen, *Opt. Express* **2016**, *24*, 6656.

[29] D. Wen, S. Chen, F. Yue, K. Chan, M. Chen, M. Ardron, K. F. Li, P. W. H. Wong, K. W. Cheah, E. Y. B. Pun, G. Li, S. Zhang, X. Chen, *Adv. Opt. Mater.* **2016**, *4*, 321.

[30] D. Wen, F. Yue, M. Ardron, X. Chen, *Sci. Rep.* **2016**, *6*, 27628.

[31] L. Huang, X. Chen, H. Mühlenbernd, G. Li, B. Bai, Q. Tan, G. Jin, T. Zentgraf, S. Zhang, *Nano Lett.* **2012**, *12*, 5750.

[32] F. Monticone, N. M. Estakhri, A. Alù, *Phys. Rev. Lett.* **2013**, *110*, 203903.

[33] K. Chen, Y. Feng, F. Monticone, J. Zhao, B. Zhu, T. Jiang, L. Zhang, Y. Kim, X. Ding, S. Zhang, A. Alù, C.-W. Qiu, *Adv. Mater.* **2017**, *29*, 1606422.

[34] L. Li, T. J. Cui, W. Ji, S. Liu, J. Ding, X. Wan, Y. B. Li, M. Jiang, C.-W. Qiu, S. Zhang, *Nat. Commun.* **2017**, *8*, 197.

[35] Y.-W. Huang, H. W. H. Lee, R. Sokhoyan, R. A. Pala, K. Thyagarajan, S. Han, D. P. Tsai, H. A. Atwater, *Nano Lett.* **2016**, *16*, 5319.

[36] K. Dong, S. Hong, Y. Deng, H. Ma, J. Li, X. Wang, J. Yeo, L. Wang, S. Lou, K. B. Tom, K. Liu, Z. You, Y. Wei, C. P. Grigoropoulos, J. Yao, J. Wu, *Adv. Mater.* **2018**, *30*, 1703878.

[37] X. Yin, T. Steinle, L. Huang, T. Taubner, M. Wuttig, T. Zentgraf, H. Giessen, *Light Sci. Appl.* **2017**, *6*, e17016.

[38] C. H. Chu, M. L. Tseng, J. Chen, P. C. Wu, Y.-H. Chen, H.-C. Wang, T.-Y. Chen, W. T. Hsieh, H. J. Wu, G. Sun, D. P. Tsai, *Laser Photon. Rev.* **2016**, *10*, 1600106.

[39] C. Choi, S.-J. Kim, J.-G. Yun, J. Sung, S.-Y. Lee, B. Lee, *Chin. Opt. Lett.* **2018**, *16*, 050009.

[40] S. M. Kamali, E. Arbabi, A. Arbabi, Y. Horie, A. Faraon, *Laser Photonics Rev.* **2016**, 10, 1002.

[41] H.-S. Ee, R. Agarwal, *Nano Lett.* **2016**, *16*, 2818.

[42] S. C. Malek, H.-S. Ee, R. Agarwal, *Nano Lett.* **2017**, *17*, 3641.

[43] X. Li, L. Chen, Y. Li, X. Zhang, M. Pu, Z. Zhao, X. Ma, Y. Wang, M. Hong, X. Luo, *Sci. Adv.* **2016**, *2*, e1601102.

[44] Q.-T. Li, F. Dong, B. Wang, F. Gan, J. Chen, Z. Song, L. Xu, W. Chu, Y.-F. Xiao, Q. Gong, Y. Li, *Opt. Express* **2016**, *24*, 16309.

[45] S. Wang, P. C. Wu, V.-C. Su, Y.-C. Lai, M.-K. Chen, H. Y. Kuo, B. H. Chen, Y. H. Chen, T.-T. Huang, J.-H. Wang, R.-M. Lin, C.-H. Kuan, T. Li, Z. Wang, S. Zhu, D. P. Tsai, *Nat. Nanotechnol.* **2018**, *13*, 227.

[46] W. T. Chen, A. Y. Zhu, V. Sanjeev, M. Khorasaninejad, Z. Shi, E. Lee, F. Capasso, *Nat. Nanotechnol.* **2018**, *13*, 220.

[47] H. Zuo, D.-Y. Choi, X. Gai, P. Ma, L. Xu, D. N. Neshev, B. Zhang, B. Luther-Davies, *Adv. Opt. Mater.* **2017**, *5*, 1700585.

[48] M. Khorasaninejad, F. Capasso, *Science* **2017**, *358*, eaam8100.

[49] H. Kikuta, Y. Ohira, H. Kubo, K. Iwata, *J. Opt. Soc. Am. A* **1998**, *15*, 1577.

[50] Z. Zhou, J. Li, R. Su, B. Yao, H. Fang, K. Li, L. Zhou, J. Liu, D. Stellinga, C. P. Reardon, T. F. Krauss, X. Wang, *ACS Photonics* **2017**, *4*, 544.

[51] P. Lalanne, P. Chavel, *Laser Photonics Rev.* **2017**, *11*, 1600295.

[52] A. She, S. Zhang, S. Shian, D. R. Clarke, F. Capasso, *Sci. Adv.* **2018**, *4*, eaap9957.

[53] F. Lu, F. G. Sedgwick, V. Karagodsky, C. Chase, C. J. Chang-Hasnain, *Opt. Express* **2010**, *18*, 12606.

[54] D. Fattal, J. Li, Z. Peng, M. Fiorentino, R. G. Beausoleil, *Nat. Photon.* **2010**, *4*, 466.

[55] K. E. Chong, I. Staude, A. James, J. Dominguez, S. Liu, S. Campione, G. S. Subramania, T. S. Luk, M. Decker, D. N. Neshev, I. Brener, Y. S. Kivshar, *Nano Lett.* **2015**, *15*, 5369.

[56] K. E. Chong, L. Wang, I. Staude, A. R. James, J. Dominguez, S. Liu, G. S. Subramania, M. Decker, D. N. Neshev, I. Brener, Y. S. Kivshar, *ACS Photoncis* **2016**, *3*, 514.

[57] X. Gai, D.-Y. Choi, B. Luther-Davies, *Opt. Express* **2014**, *22*, 9948.

[58] R. Paniagua-Domínguez, Y. F. Yu, E. Ehaidarov, S. Choi, V. Leong, R. M. Bakker, X. Liang, Y. H. Fu, V. Valuckas, L. A. Krivitsky, A. I. Kuznetsov, *Nano Lett.* **2018**, *18*, 2124.

[59] A. Arbabi, Y. Horie, A. J. Ball, M. Bagheri, A. Faraon, *Nat. Commun.* **2015**, *6*, 7069.

[60] B. H. Chen, P. C. Wu, V.-C. Su, Y.-C. Lai, C. H. Chu, I. C. Lee, J.-W. Chen, Y. H. Chen, Y.-C. Lan, C.-H. Kuan, D. P. Tsai, *Nano Lett.* **2017**, *17*, 6345.

[61] A. Zhan, S. Colburn, R. Trivedi, T. K. Fryett, C. M. Dodson, A. Majumdar, *ACS Photonics* **2016**, *3*, 209.

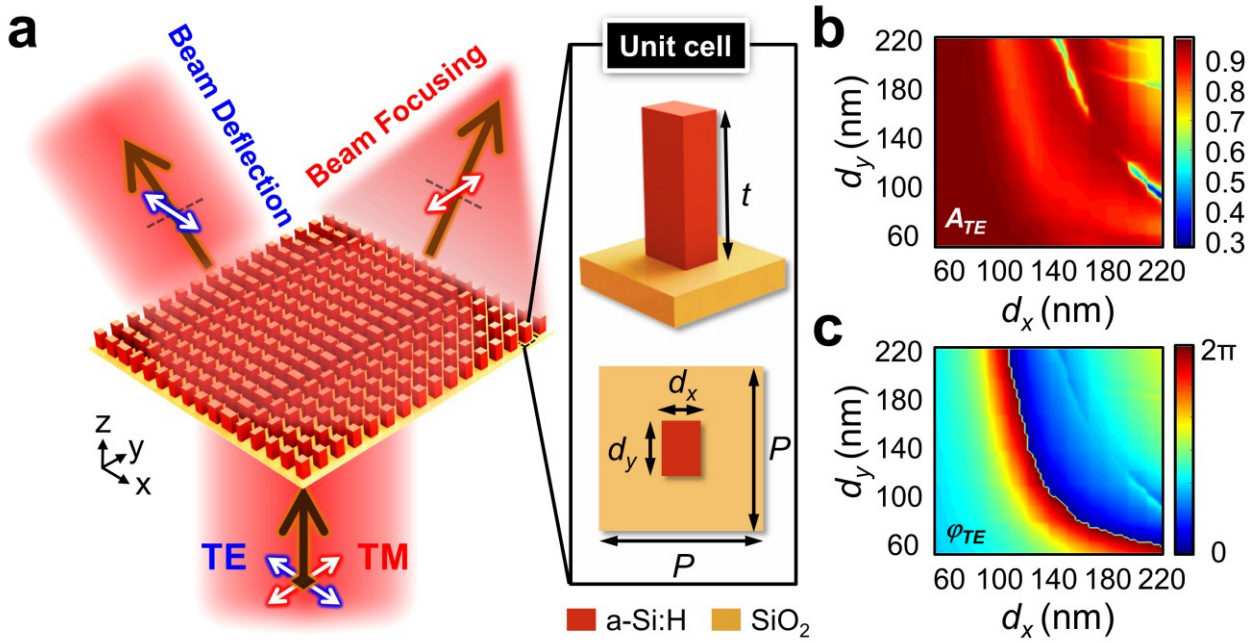

Figure 1. (a) Schematic of the proposed highly efficient bifunctional metasurface enabling polarization-tuned focusing and deflection for visible light. Shown on the right side is the metasurface UC, incorporating the a-Si:H nanopost. Calculated (b) amplitude and (c) phase distribution as a function of the cross-sectional dimension of the nanopost for TE polarization at the designed wavelength of λ_0 = 690 nm.

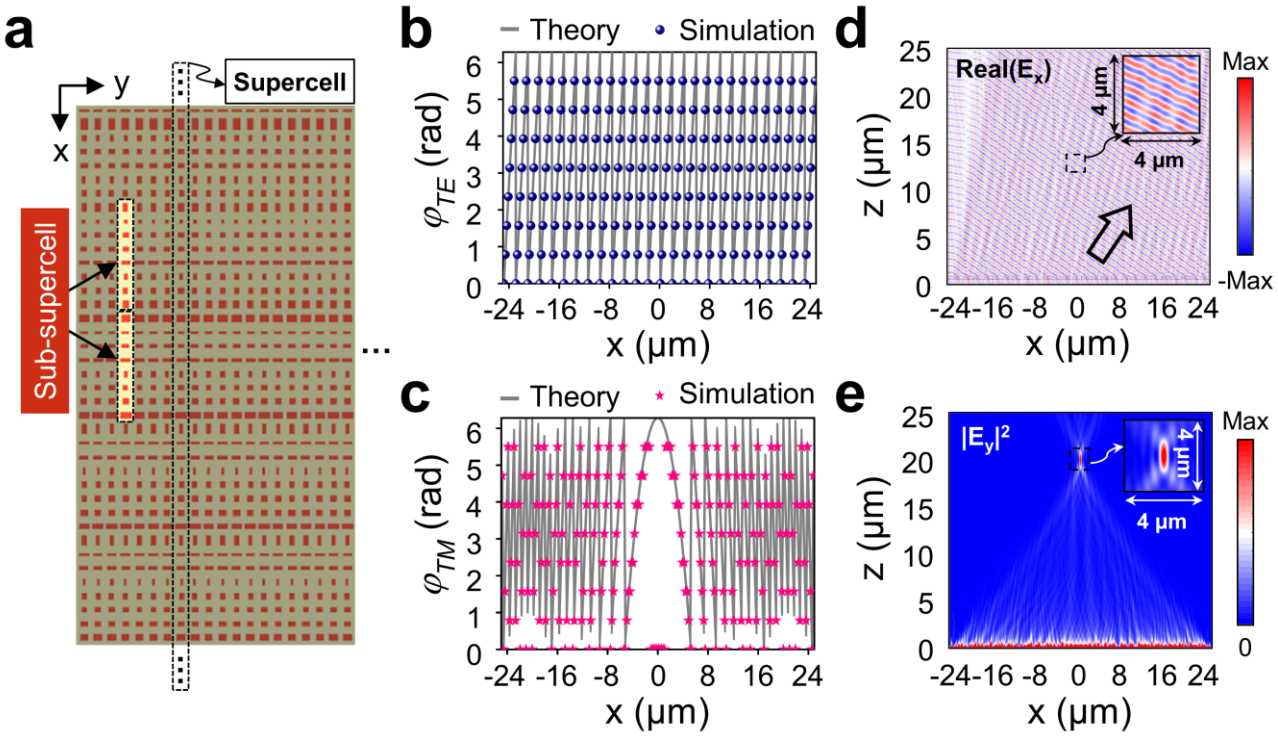

Figure 2. (a) Schematic showing the arrangement of the nanoposts in the designed bifunctional metasurface. The theoretical and simulated phase profiles for (b) beam deflection under normal TE incidence and (c) beam focusing under normal TM incidence. (d) The x-component of the transmitted electric field under normal TE incidence. (e) The y-component of the transmitted field intensity under normal TM incidence.

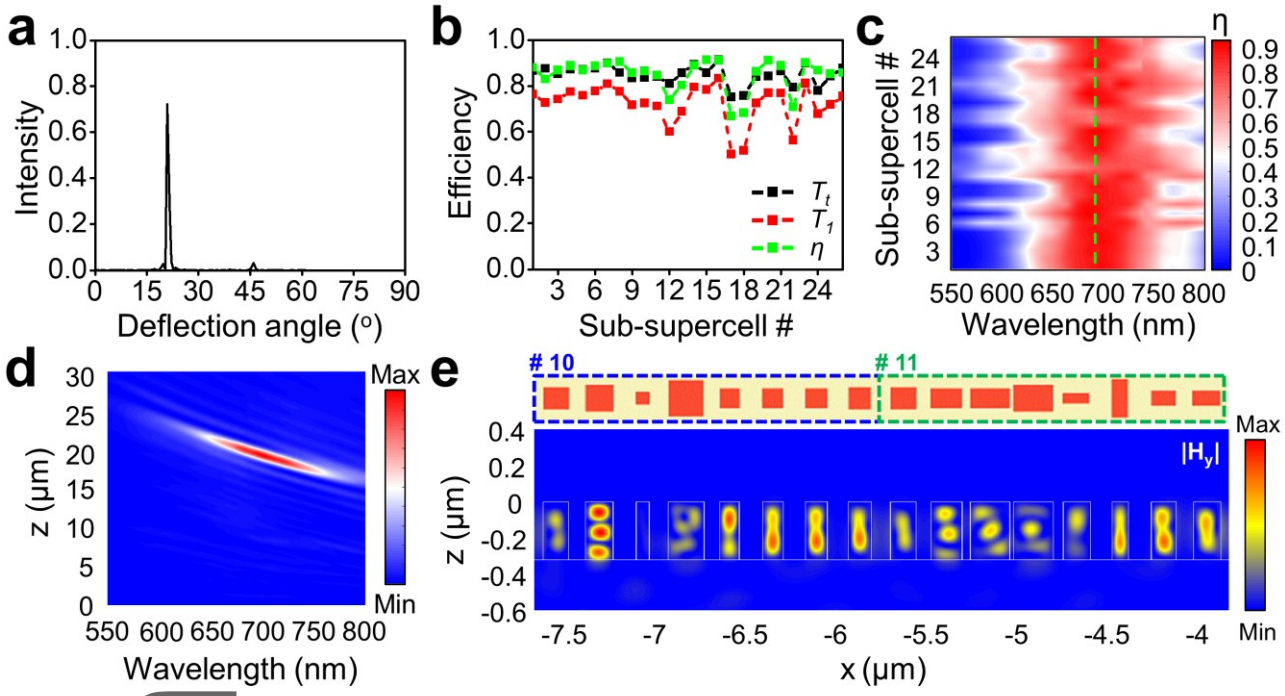

Figure 3. (a) Normalized far-field intensity as a function of the transmission angle at the wavelength of λ_0 = 690 nm under normal TE incidence. (b) The simulated total transmission (T), absolute (T_1), and relative (η) deflection efficiency for the 26 sub-supercells under normal TE incidence. (c) The simulated relative deflection efficiency in a broad spectral band for the 26 sub-supercells. (d) The simulated field intensity distribution along the z-axis at the center (x = 0) of the bifunctional metasurface, as a function of the wavelength under TM incidence. (e) The $|H_y|$ field distribution in the x-z plane at the designed wavelength for two sub-supercells (# 10 and # 11).

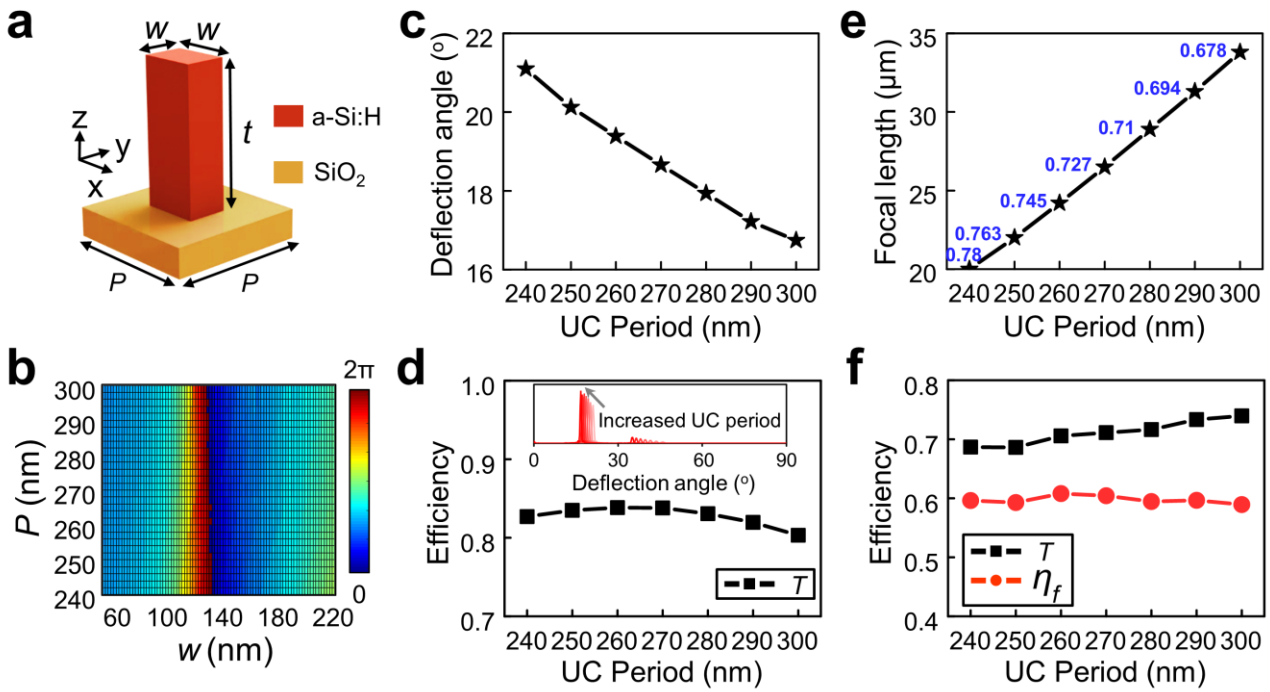

Figure 4. (a) Schematic of a metasurface UC incorporating nanopost exhibiting identical widths. (b) Transmitted light phase distribution in terms of the UC periodicity and the nanopost dimension. Effect of the UC periodicity on the performance of the bifunctional metasurface in terms of (c) the deflection angle and (d) total transmission under normal TE incidence; (e) focal length and (f) total transmission and focusing efficiency under normal TM incidence. Inset in Figure 4d shows the simulated far-field intensity with the transmission angle through varying UC periodicity.

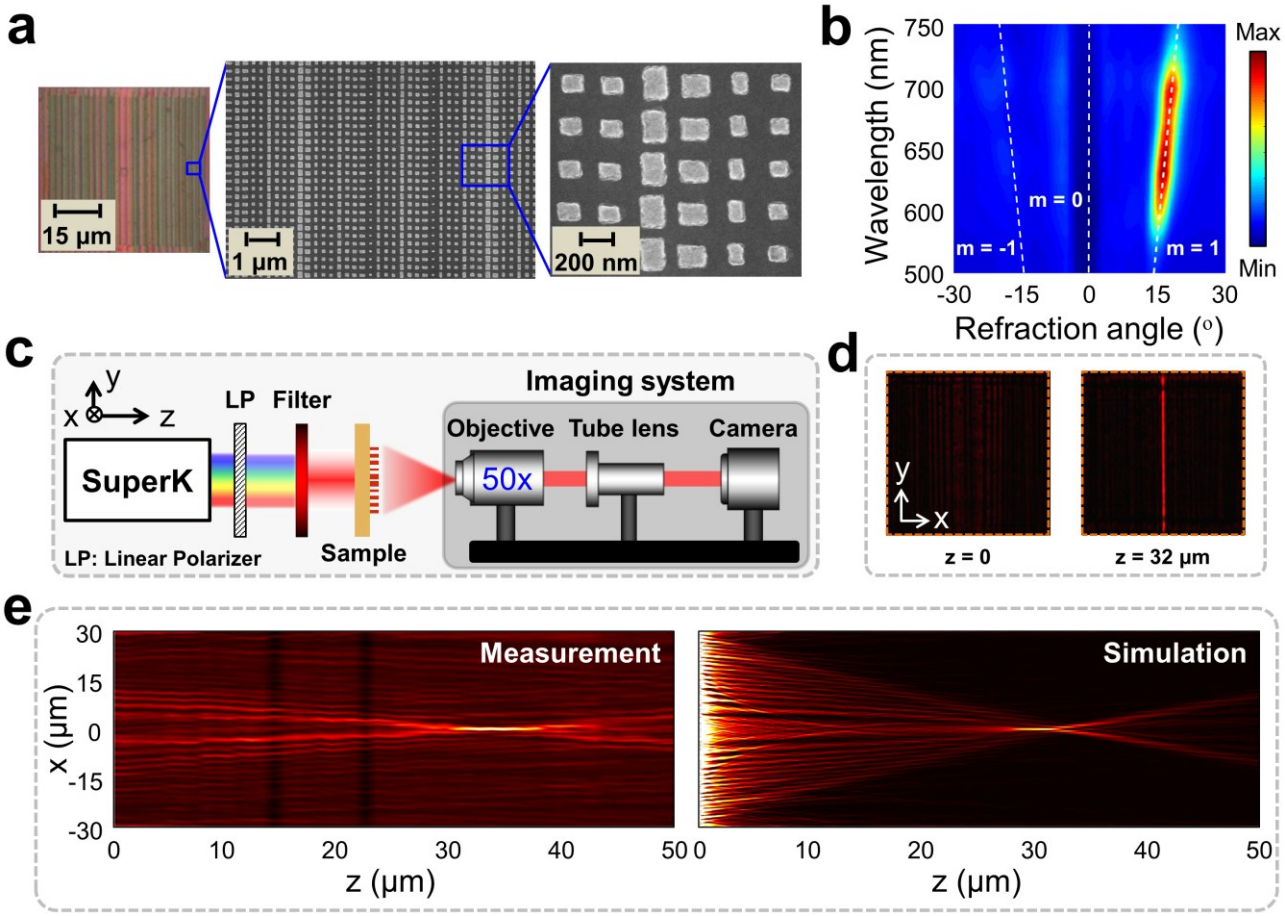

Figure 5. (a) Optical image and SEM image of the fabricated metasurface. (b) Measured normalized far-field intensity with respect to the transmission angle and wavelength for normal TE incidence. (c) Test setup for obtaining the light intensity profile in the x-y plane for TM incidence. (d) Observed optical images at the sample surface (z = 0) and the focal plane (z ≈ 32 μm). (e) Extracted intensity profile in the x-z plane in experiment and simulation.

ToC figure ((Please choose one size: 55 mm broad × 50 mm high **or** 110 mm broad × 20 mm high.))

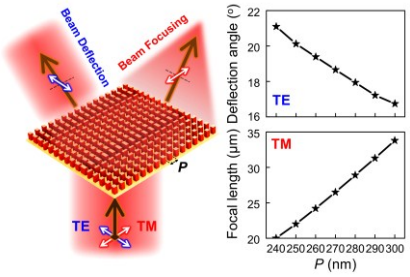

A highly efficient bifunctional dielectric metasurface capitalizing on the rectangular a-Si:H nanoposts as the building blocks, has been proposed and developed to enable polarization-tuned anomalous beam deflection and focusing for visible light. Through the tailoring of the unit cell periodicity, we are capable of efficiently tuning the beam deflection angle and focusing distance.